RSC Advances

ROYAL SOCIETY OF CHEMISTRY

PAPER

View Article Online
View Journal | View Issue

Check for updates

Cite this: *RSC Adv.*, 2024, **14**, 17355

Optically compatible infrared camouflage performance of ITO ink†

Xiao Feifei,* Xu Weidong, Liu Heng, Li Hao, Yu Haibao and Hao Bentian

With the rapid development of military reconnaissance technology, reconnaissance devices have been equipped with wideband reconnaissance ability, which imposes increased requirements on camouflage. Developing multiband camouflage materials with good compatibility has become increasingly important. Indium tin oxide (ITO), a transparent conductive oxide with good comprehensive photoelectric properties, exhibits different absorption, reflectivity, and transmission characteristics in different bands of electromagnetic waves. Therefore, ITO might be able to solve broadband and multiband camouflage problems effectively. In this paper, ITO is expressed as $In_{32-x}Sn_xO_{48}$. The energy band structure, optical properties, and infrared absorption spectra at different doping ratios of Sn ($x = 0, 1, 2, 3$) were obtained on the basis of first principle theory, and the camouflage mechanism of ITO in different electromagnetic wavebands was explored. Results demonstrated that when $x = 3$, specifically, when the doping ratio of Sn atoms was 9.375%, ITO had high transmission in the visible light band and infrared band reflectivity and can realize optically compatible infrared camouflage. In accordance with calculation results, ITO nanodispersion liquid ($x = 3$) was mixed with green camouflage coating added with some additives to prepare green ITO camouflage ink for silkscreen printing. The ink formed a camouflage protective ink coating after it was coated onto the surface of fabric through silkscreen printing. Results showed that the emissivity of the ITO ink coating decreased by more than 0.13 when its solid content reached 20%, and its camouflage performance in the visible light band was barely affected. The results of this research can guide the application of ITO materials in the field of camouflage.

Received 15th April 2024
Accepted 23rd May 2024

DOI: 10.1039/d4ra02784a

rsc.li/rsc-advances

1. Introduction

Under modern war conditions and severe threats from high-technology reconnaissance and surveillance, good camouflage protection is particularly important for sudden attacks and maintaining target survival on the battlefield. Developing multispectral camouflage materials covering optics, infrared, and radar wavebands on the basis of existing camouflage materials is necessary. Camouflage blankets and covers should be fabricated on the basis of camouflage fabrics and in accordance with the typical geological background and camouflage needs of targets. Through the adjustment of multiple technologies and combined design of multispectral camouflage, targets can be easily hidden and their importance can be reduced, thus providing technological support for the comprehensive camouflage of targets.[1–3] Camouflage fabrics have the characteristics of strong flexibility, light weight, and easy transportability. However, existing camouflage fabrics have poor adaptation to different environments and are insufficiently light. Existing camouflage fabrics should be changed continuously in accordance with the war environment to improve camouflage efficacy.[4,5] The real-time production of camouflage patterns that integrate well with the background environment and coating of optically compatible infrared camouflage ink onto the surfaces of camouflage fabric through silkscreen printing can make targets blend with the background color and surface tissue structure, develop deformation in the infrared band, and realize optical and infrared camouflage functions.[6,7] The key material of optically compatible infrared camouflage ink is the functional fillers that can reduce the emissivity of the coating without damaging its optical camouflage function.

Indium tin oxide (ITO), a transparent conductive oxide with good comprehensive photoelectric properties, can absorb, reflect, and transmit different bands of electromagnetic waves. ITO, which has the potential for multispectral camouflage, is expected to be used as a functional filler in multispectral compatible inks. ITO is mainly applied in the form of thin films in various industries. In 1984, Schott Glaswerke demonstrated that ITO film formed on a PET base has high reflectivity at 9.5 μm, high visible light permeability, good adhesion force with glass on base plates, high anti-scratching property, and good weather resistance.[8] Similar conclusions have been drawn in subsequent studies. The preparation of ITO thin film faces great

---

Field Engineering College, Army Engineering University of PLA, Nanjing 210014, China. E-mail: xiaofeieif8719@126.com

† Electronic supplementary information (ESI) available. See DOI: https://doi.org/10.1039/d4ra02784a

challenges and incurs a high cost, which restricts its application in camouflage projects. The application of ITO as a camouflage ink might be suitable for camouflage protection projects. Some studies on the applications of ITO in transparent thermal insulation coating and nanoprinting ink have been reported. Although relevant studies have demonstrated that ITO has good transparency in the optical band, its absorption, reflectivity, and transmission mechanisms of infrared electromagnetic waves have different interpretations.[9–11] ITO is obtained by doping In_2O_3 with Sn. The addition of Sn influences the physical properties of materials remarkably and determines the performance of ITO. Given that each Sn atom can only provide a maximum of one excessive electron to In_2O_3, a sufficiently high Sn density is required to obtain numerous charge carriers (electrons).[10] Thus far, ITO has been applied in practical engineering through heavy doping.

In_2O_3 has a ferromanganese structure that contains 80 atoms, including 32 indium atoms and 48 oxygen atoms. The chemical formula of In_2O_3 after being doped with Sn can be defined as $In_{32-x}Sn_xO_{48}$, where x represents the number of added Sn atoms. The material structure can influence the basic physical and chemical properties of $In_{32-x}Sn_xO_{48}$. In this study, the geometric structure of the dominant crystal of $In_{32-x}Sn_xO_{48}$, which contains 80 atoms, was optimized on the basis of first principle theory. In addition, the energy band structure, optical properties, and infrared adsorption spectra of the crystal when $x = 0, 1, 2, 3$ (representing Sn atom doping ratios of 0%, 3.125%, 6.25%, and 9.375%) were calculated to characterize the properties of ITO materials. This study aims to explore the camouflage mechanism of ITO in different electromagnetic bands. Additionally, ITO with the optimal comprehensive performance was chosen in accordance with calculation results. The nanodispersion liquid of the chosen ITO was mixed with green optical camouflage coating to prepare ink film on high-strength polyester fabric surfaces through silkscreen printing. The camouflage performances of the ink film compatible with the visible light and infrared bands were investigated.

2. Methods

2.1 Calculation in accordance with first principle theory

In this study, first principle theory based on density functional theory (DFT) was chosen and applied by using the CASTEP calculation program.[12] The crystal structure used in this study contained 80 atoms. Geometric structural optimization and property calculation require considerable calculation loads. We first conducted a convergence test on the K point and truncation energy of the plane wave to balance calculation loads and accuracy. In the test, the K point was $4 \times 4 \times 4$, the truncation energy of the plane wave was 600 eV, and the convergence standard was 10 meV per atom.[13,14]

The first step of calculation has to optimize the geometric structure of crystals to guarantee the accuracy of subsequent calculations. In this study, LBFGS was employed as the geometric optimization algorithm, and the DFT method was based on generalized gradient approximation (GGA) and Perdew–Burke–Ernzerhof (PBE).[15] The dispersion correction method used TS. Spin and spin–orbit coupling were open during the geometric structural optimization of crystals.[16] The judgment criteria for ion step convergence were set as follows: an energy of 5.0×10^{-6} eV per atom, a max.force of 0.01 eV $Å^{-1}$, a max.stress of 0.01 GPa, and a max.displacement of 5.0×10^{-4} Å. Crystal optimization used full mode. At electron step convergence, pseudopotentials used norm conserving.[17] The convergence standards were set as an SCF tolerance of 5.0×10^{-7} eV per atom and max.SCF cycles of 100.

For the optimized crystal structure, spin tended to be 0 and was ignored in the subsequent calculation of properties. The energy band structure and optical properties of crystals along the four high symmetric point paths in the Brillouin zone were calculated with the GGA and HSE06 hybrid functions.[18–20] The infrared absorption spectra of crystals were obtained by using the original crystal structure and involved the strict optimization of geometric structures. In this case, the criteria for ion step convergence were stricter than those of ordinary geometric structural optimization, as follows: an energy of 2.0×10^{-6} eV per atom, a max.force of 0.002 eV $Å^{-1}$, a max.stress of 0.004 GPa, and a max.displacement of 2.0×10^{-4} Å. The other convergence criteria were consistent with the convergence criteria used during geometric structure optimization.

For $In_{32-x}Sn_xO_{48}$, all calculations focused on the In_2O_3 structure when $x = 0$. Calculation was implemented in accordance with the above methods. When $x = 1, 2, 3$, the calculation focused on the ITO structure with different Sn doping ratios. Doping processing was performed with the disorder script (See Appendix – Disorder script) by using the optimized In_2O_3 as the input structure. After doping, another geometric structural optimization was conducted on the structure added with Sn. As a result of heavy doping, the doping ratio of Sn was high, and the point O was ignored during calculation.[21] Sn atoms were added into defect-free crystals to simulate In_2O_3 with different point defects caused by various doping ratios.[22] The dominant crystals of $In_{32-x}Sn_xO_{48}$ containing 80 atoms had two Wyckoff sites of 8b and 24d. A total of 32 configurations existed when $x = 1$. Two different configurations were obtained after simplification. When $x = 2$, 496 configurations were present, and 18 different configurations were identified after simplification. When $x = 3$, 4312 configurations were present, and 100 different configurations were identified after simplification. The single-point energy of different configurations when $x = 1, 2, 3$ was calculated. The three structures with the lowest single-point energy among all structures were identified for the optimization of geometric structures. Symmetry was not added during the geometric optimization of all configurations to avoid reducing symmetry. In accordance with the geometric optimization results, the structure with the lowest and the most stable energy among all structures was chosen as the final structure. The calculation method for ITO was consistent with that for In_2O_3.

2.2 Preparation and performance characterization of ITO silkscreen printing ink

In accordance with the calculation results, ITO nanodispersion liquid with the corresponding doping ratios were mixed with the same medium green camouflage coating ($L = 39.58$, $a = -6.37$, $b = 17.01$) at the ITO solid contents of 10%, 20%, and 30%. They were mixed mechanically for 1 h in a SDF400 laboratory multipurpose dispersion sand mill at the rate of 400 rpm. An appropriate amount of retarder (mass ratio of isohexadiol : water = 1 : 1) and thickener (mass ratio of PMA : M240 : H_2O = 1 : 1 : 1) were added to the coating in the uniform dispersion. The solution was adjusted to the state appropriate for silkscreen printing. The ITO silkscreen printing ink was prepared in this manner. The prepared ink was printed onto the surface of high-strength polyester fabric by using a customized scraper and 80-, 120-, and 200-mesh screen printing plates. The fabric was held still until the ink film dried and then dried in a drying oven at 50 °C for 1 h. The optical chromatic value and color difference of the ink film were tested with an UltraScan Pro spectrophotometer. The emissivity of the ink film at 8–14 μm was measured by using an IR-2 double-band emissivity meter.

3. Results and discussion

3.1 First principle theory calculation results

3.1.1 Crystal structure. At room temperature and normal pressure, the stable structure of In_2O_3 is a corundum-like cubic structure, that is, c-ITO. In_2O_3 is Corundum-like structured and crystallizes in the cubic $Ia\bar{3}$ space group. In_2O_3 has two unequal In^{3+} sites. At the first In^{3+} site, In^{3+} binds with six equivalent O^{2-} atoms, forming a distorted InO_6 octahedral mixture with common angles and sides. The dip angles of the octahedron range from 54° to 55°. The distribution range of the In–O bond distance is 2.14–2.23 Å. At the second In^{3+} site, In^{3+} forms bonds with six equivalent O^{2-} atoms, forming an InO_6 octahedral mixture with common angles and sides. The dip angle of the octahedron is 54°. The length of all In–O bonds is 2.19 Å. O^{2-} forms bonds with four In^{3+} atoms, forming a distorted In_4 triangular pyramid mixture with common sides and angles. In_2O_3 after geometric structural optimization is shown in Fig. 1(a), wherein red atoms are O atoms and brown atoms are In atoms.

When $x = 1$, one Sn^{4+} replaces one In^{3+} site, and crystal distortion occurs when Sn is introduced into the In_2O_3 crystal; Sn^{4+} is prone to entering b^+ sites with a low degree of distortion.[23,24] Given the high doping content of Sn, the crystal structure remains unchanged. When $x = 2, 3$, the crystal structure of ITO remains consistent with that of c-ITO, as has been proved by calculations.[25] ITO after geometric structural optimization at $x = 1$, 2, 3 is shown in Fig. 1(b)–(d), wherein the lake blue atoms are Sn atoms added into the In_2O_3 crystal.

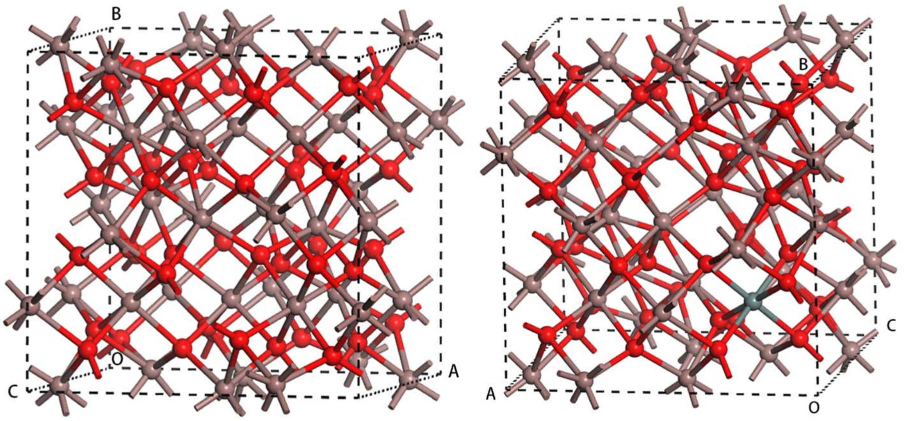

(a) In_2O_3 (b) $In_{31}Sn_1O_{48}$

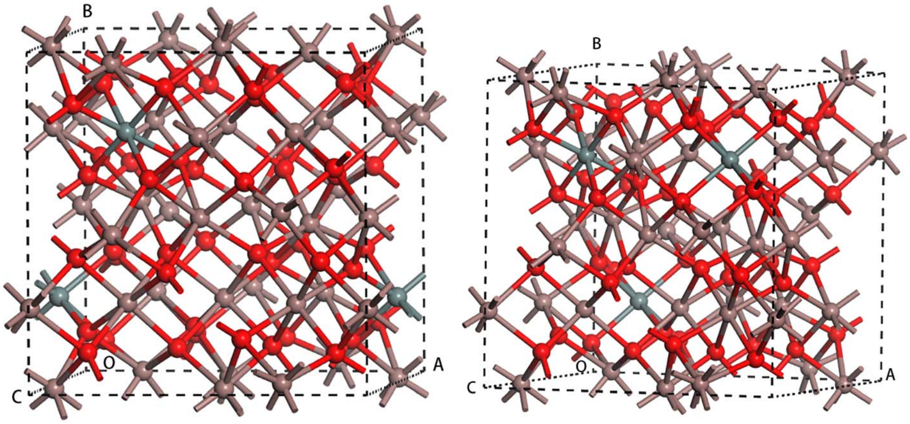

(c) $In_{30}Sn_2O_{48}$ (d) $In_{29}Sn_3O_{48}$

Fig. 1 Crystal structure of $In_{32-x}Sn_xO_{48}$ with (a) In_2O_3; (b) $In_{31}Sn_1O_{48}$; (c) $In_{30}Sn_2O_{48}$ and (d) $In_{29}Sn_3O_{48}$.

3.1.2 Band structure.

The CASTEP program calculates the band structure of crystals in accordance with the crystal structure and highly symmetric point paths in the Brillouin zone. The band structure of $In_{32-x}Sn_xO_{48}$ is shown in Fig. 2.

In Fig. 2, the dotted line with the energy of 0 represents the Fermi level. The HSE06 hybrid function was applied for calculation before Sn doping. The energy band gap of In_2O_3 is the direct band gap and has a value of 2.985 eV. After doping with Sn at different ratios, the energy band structure of ITO negligibly changes. With the increase in doping ratio, the Fermi level moves deeply into the conduction band, whereas the optical band gap expands gradually. The maximum optical energy gap exceeds 4 eV when $x = 3$, which can guarantee the transparency of the whole visible spectra. The expansion width of the optical band gap could be interpreted in accordance with Burstein–Moss mobility theory.[26]

The high-valence Sn^{4+} in ITO replaces the In^{3+} site, thus increasing carrier concentration. The Fermi level enters the conduction band completely or partially. Some energy levels at the bottom of the conduction band are occupied by electrons. Therefore, electrons can only jump from a position in the valence band to the lowest energy state of the conduction band that has not been occupied by electrons. In other words, the effective optical energy gap of samples widens, thus making the practical absorption spectra move toward the short-wave direction. However, the electron wave function of impurity atoms exhibit considerable overlaps with the continuous increase in Sn content. The energy level of isolated impurities expands into an energy band that connects to the bottom of the conduction band to form a new degenerate conduction band with the tail extending into the forbidden band. This phenomenon narrows the original forbidden band.

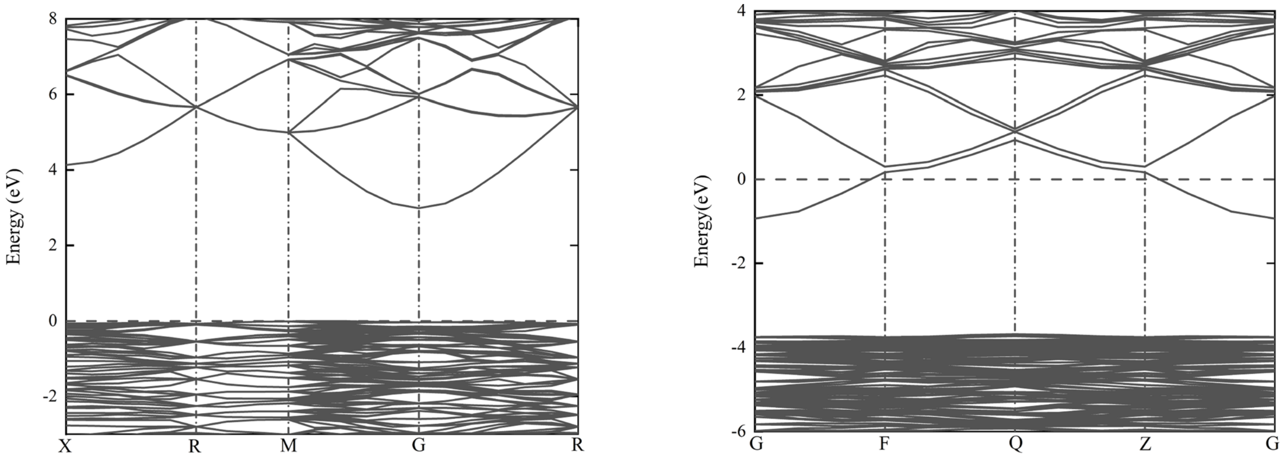

(a) In_2O_3 (b) $In_{31}Sn_1O_{48}$

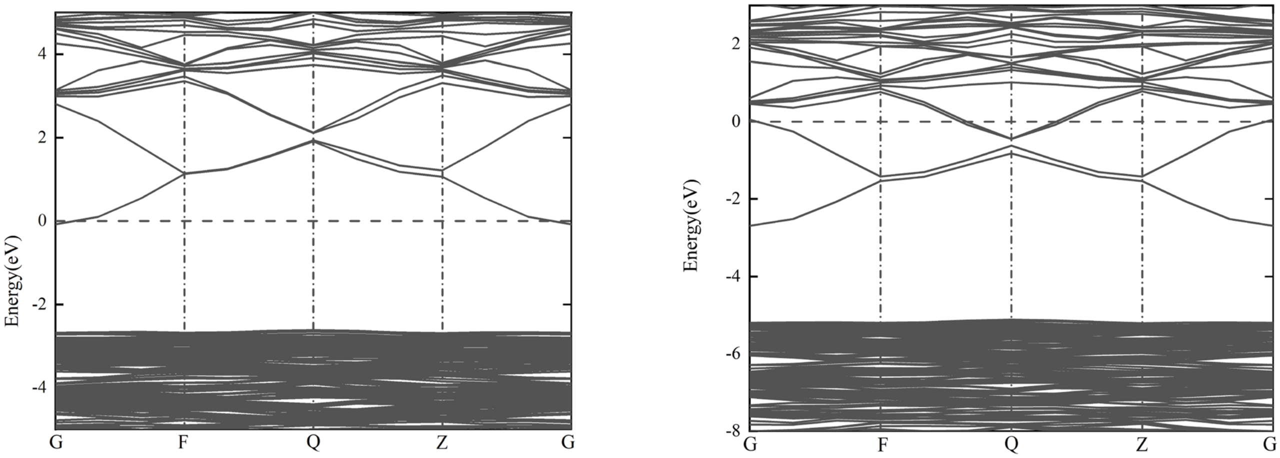

(c) $In_{30}Sn_2O_{48}$ (d) $In_{29}Sn_3O_{48}$

Fig. 2 Band structure of $In_{32-x}Sn_xO_{48}$ with (a) In_2O_3; (b) $In_{31}Sn_1O_{48}$; (c) $In_{30}Sn_2O_{48}$ and (d) $In_{29}Sn_3O_{48}$.

The macroscopic electrical properties of materials are mainly decided by the properties of the electrons near the Fermi surface. When $x > 0$, the Fermi level enters the conduction band, indicating that free electrons are present near the Fermi level. With the increase in doping ratio, the Fermi level increases gradually, as can be proven by the calculated state density (Fig. 3, wherein the dotted line with the energy of 0 is the Fermi level). The high Fermi level indicates the strong electrical conductivity of ITO. When $x = 3$, the Fermi level enters the conduction band deeply and is far from the bottom of the conduction band. Electrons near the Fermi level can only jump among dense energy levels in the conduction band but undergo forbidden transition among forbidden bands. All of these phenomena are similar to metal characteristics and may account for the low emissivity of ITO in the infrared band.

3.1.3 Optical properties. The CASTEP calculation of optical properties was conducted in accordance with linear response theory. This method can be used to calculate various properties, including the real part $\varepsilon_1(\omega)$ and virtual part $\varepsilon_2(\omega)$ of the dielectric function, reflectivity $R(\omega)$, absorption coefficient $\alpha(\omega)$, and electron energy loss function $L(\omega)$. ω expresses the frequency of incident electromagnetic waves.

The real part of the dielectric function expresses polarization caused by external electromagnetic field and characterizes the contributions of media to light adsorption. The virtual part expresses media dissipation in the electric field. They are the most fundamental optical properties, and other properties can be calculated from the dielectric function. The calculation formulas for reflectivity $R(\omega)$, absorption coefficient $\alpha(\omega)$, and

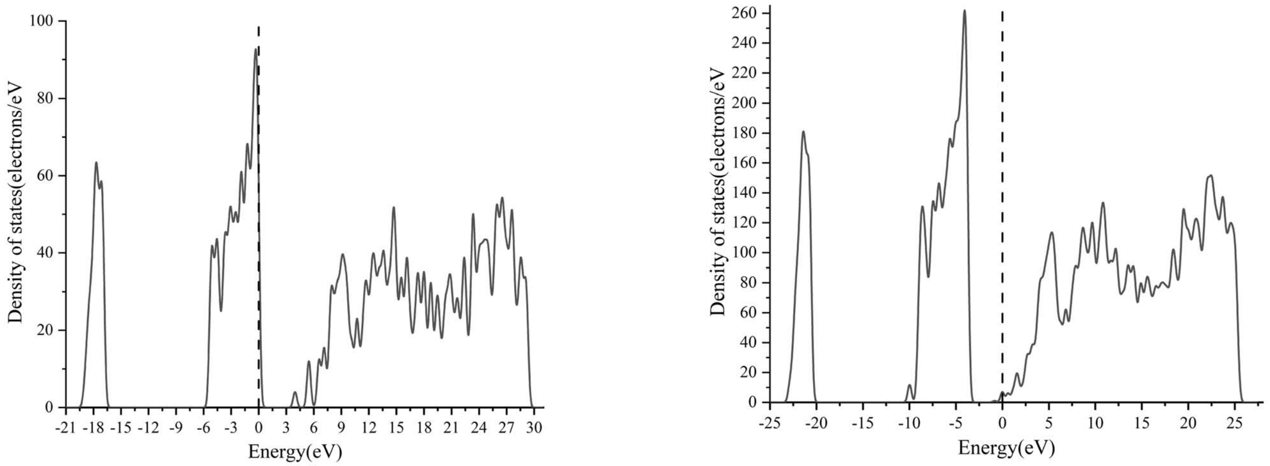

(a) In_2O_3 (b) $In_{31}Sn_1O_{48}$

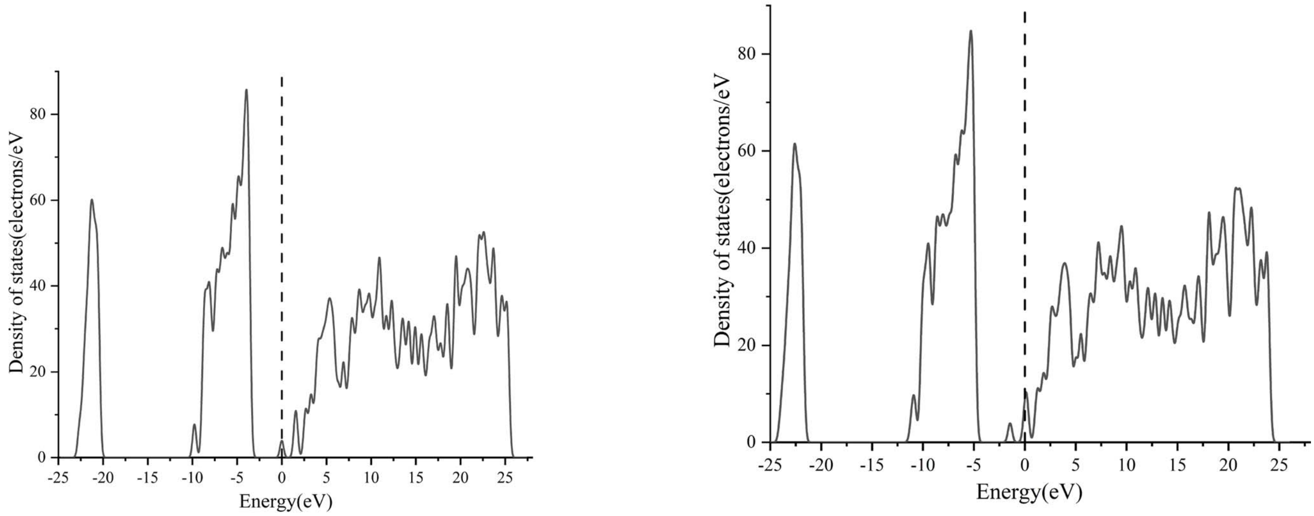

(c) $In_{30}Sn_2O_{48}$ (d) $In_{29}Sn_3O_{48}$

Fig. 3 Density of states of $In_{32-x}Sn_xO_{48}$ with (a) In_2O_3; (b) $In_{31}Sn_1O_{48}$; (c) $In_{30}Sn_2O_{48}$ and (d) $In_{29}Sn_3O_{48}$.

electron energy loss function $L(\omega)$ are shown as eqn (1)–(3), respectively.

$$R(\omega) = \left|\frac{\sqrt{\varepsilon_1(\omega) + j\varepsilon_2(\omega)} - 1}{\sqrt{\varepsilon_1(\omega) + j\varepsilon_2(\omega)} + 1}\right|^2, \tag{1}$$

$$\alpha(\omega) = \sqrt{2}\omega + \left[\sqrt{{\varepsilon_1}^2(\omega) + {\varepsilon_2}^2(\omega)} - \varepsilon_1(\omega)\right]^{1/2}, \tag{2}$$

$$L(\omega) = \varepsilon_2(\omega)/[{\varepsilon_1}^2(\omega) + {\varepsilon_2}^2(\omega)]. \tag{3}$$

The optical properties of $In_{32-x}Sn_xO_{48}$ obtained through calculation are shown in Fig. 4, wherein the x-axis has been transformed into wavelength (nm).

Fig. 4 shows that when $x = 1, 2$, the optical properties of $In_{32-x}Sn_xO_{48}$ change slightly relative to those of In_2O_3. When $x = 3$, Sn concentration increases and provides additional free electrons. Therefore, ITO becomes a high-density free electron gas material because it has a high concentration of free carriers, and its response to the electromagnetic field of light (light field) is closely related to the frequency of the light field (wavelength).[27] At low frequencies, free electrons in each half cycle of the alternating light field are impacted in accelerating mode several times by the electric field along a direction. Such polarized free electron gas provides a strong shielding effect against the electromagnetism of the light field. Therefore, materials have strong reflectivity (R) in the low-frequency infrared zone. When the light frequency increases to the plasma frequency (ω_p), the inertia of electrons cannot follow the light field of high-frequency changes. Such plasma electrons have weak absorption and reflectivity in the light field, thus making the material enter the transparency zone.

When the light frequency further increases to the intrinsic excitation absorption frequency (ω_g), photons have sufficient energy to make the bound electrons of the material jump from the intrinsic band to the excitation state and become free electrons. The absorption of shortwaves with light frequency higher than ω_g has strengthened dramatically, whereas the transmittance (T) and reflectivity (R) of these shortwaves have weakened considerably.

The wavelength corresponding to the plasma frequency (ω_p) is the plasma wavelength (λ_p) and that corresponding to the intrinsic excitation (absorption) frequency (ω_g) is the intrinsic excitation wavelength (λ_g). The former is the starting point for materials to enter the high infrared reflection ($\lambda > \lambda_p$) region and also the turning point for materials to enter the low absorption and high reflection regions gradually ($\lambda < \lambda_p$). The latter is the turning point for ITO material to enter the high absorption region ($\lambda < \lambda_g$). Fig. 4 shows that for ITO, $\lambda_p \approx 1200$ nm and $\lambda_g \approx 303$ nm. The λ_g–λ_p range of ITO covers the visible light band and guarantees the transmission of ITO materials in the visible light band. Moreover, the ITO material has strong absorption in the ultraviolet region and strong reflectivity in the infrared region.

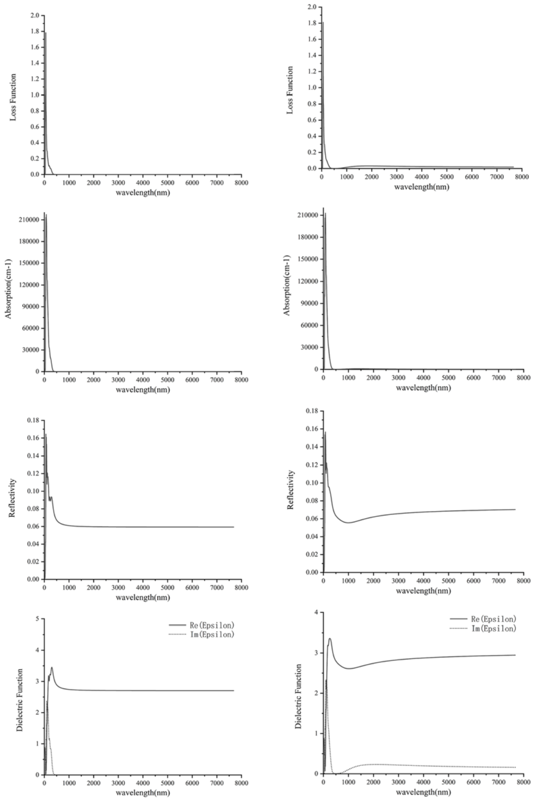

(a) In_2O_3 (b) $In_{31}Sn_1O_{48}$

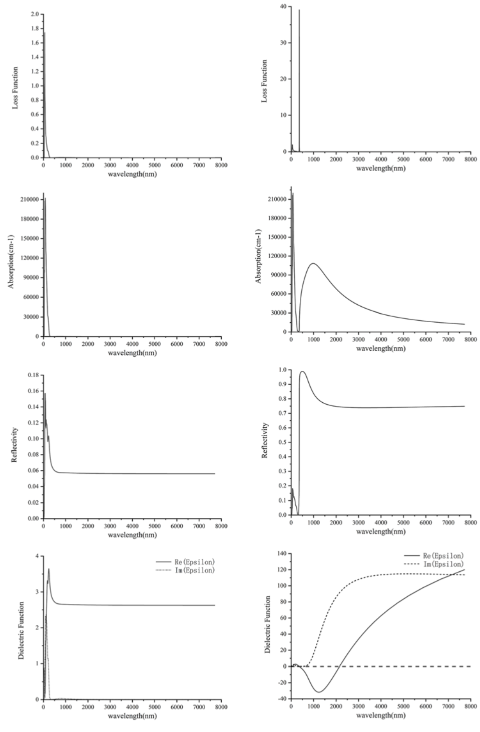

(c) $In_{30}Sn_2O_{48}$ (d) $In_{29}Sn_3O_{48}$

Fig. 4 Optical properties of $In_{32-x}Sn_xO_{48}$ with (a) In_2O_3; (b) $In_{31}Sn_1O_{48}$; (c) $In_{30}Sn_2O_{48}$ and (d) $In_{29}Sn_3O_{48}$.

3.1.4 Infrared absorption spectra. The analysis of energy band structure and optical properties shows that the Fermi level of $In_{32-x}Sn_xO_{48}$ begins to enter the conduction band and the carrier concentration is insufficient when x increases from 0 to 1 and 2. The high transmission of In_2O_3 in the visible light band is maintained. However, In_2O_3 lacks high reflectivity in the low-

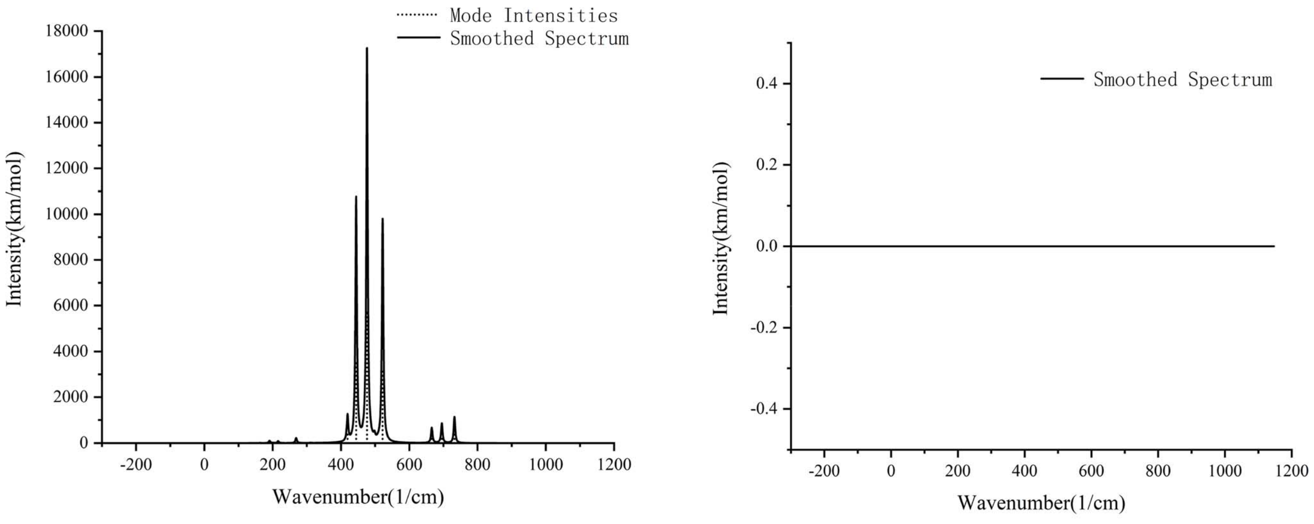

(a) In_2O_3 (b) $In_{29}Sn_3O_{48}$

Fig. 5 IR spectrum of $In_{32-x}Sn_xO_{48}$ with (a) In_2O_3 and (b) $In_{29}Sn_3O_{48}$.

frequency infrared band. When $x = 3$, the Fermi level enters the conduction band deeply and the optical band gap widens gradually. The maximum optical energy band gap exceeds 4 eV. This effect can assure transparency throughout the whole visible light spectra. Given the high concentration of free carriers, the ITO material has strong reflectivity in the low-frequency infrared region. The infrared absorption spectra of crystals at $x = 0$ and $x = 3$ were calculated on the basis of first principle theory. The results are shown in Fig. 5.

The spectral absorption characteristics of In_2O_3 and $In_{29}Sn_3O_{48}$ in the waveband ranges of 111.50–769.90 and 104.05–742.54 cm^{-1}, respectively, were calculated in accordance with first principle theory (Fig. 5). In_2O_3 has strong infrared adsorption at 444.38, 476.3, and 522.1 cm^{-1}, whereas $In_{29}Sn_3O_{48}$ has almost 0 absorption in the whole infrared waveband. Kirchhoff's radiation law states that the reflectivity and absorptivity of any object on a wavelength, an angle, and a polarization direction are equal under the balanced state.[28] The calculation results in Fig. 5 confirm that ITO has low emissivity in the far infrared band.

3.2 Optical and infrared performances of ITO silkscreen printing ink

Color difference (ΔE) was used to characterize the color deviation degree between the ink film and standard color. $\Delta E \leq 3$ is usually required. The color difference formula in the CIE1976$L^*a^*b^*$ colorimeter system was applied to evaluate the optical camouflage performances of ITO ink. The formula for calculating color difference is[29]

$$\Delta E^*_{\mathrm{ab}} = \left[(\Delta L^*)^2 + (\Delta a^*)^2 + (\Delta b^*)^2\right]^{\frac{1}{2}}, \tag{4}$$

where ΔL^*, Δa^*, and Δb^* refer to the differences between the color coordinates (L^*, a^*, and b^*) of ink film from those of medium green optical camouflage paint.

Table 1 Chromaticity and 8–14 μm emissivity values of ITO screen printing ink

Num.	Mesh count	Solid content of ITO	L	a	b	ΔL	Δa	Δb	E (8–14 μm)
1	80	0	39.06	−8.79	15.23	0.07	0.25	−0.14	0.921
2	120	0	38.94	−9.07	15.42	−0.05	−0.03	0.05	0.939
3	200	0	38.82	−8.91	15.37	−0.17	0.13	0.00	0.938
4	80	10%	38.73	−8.96	14.33	−0.26	0.08	−1.04	0.773
5	120	10%	38.72	−8.88	14.23	−0.27	0.16	−1.14	0.782
6	200	10%	38.63	−8.69	14.19	−0.36	0.35	−1.18	0.789
7	80	20%	39.69	−7.77	13.96	0.70	1.27	−1.41	0.742
8	120	20%	38.14	−8.82	14.39	−0.85	0.22	−0.98	0.744
9	200	20%	38.39	−8.54	14.57	−0.60	0.50	−0.80	0.757
10	80	30%	37.64	−8.51	12.29	−1.35	0.53	−3.08	0.763
11	120	30%	37.62	−8.60	12.43	−1.37	0.44	−2.94	0.779
12	200	30%	37.68	−8.74	12.66	−1.31	0.30	−2.71	0.793

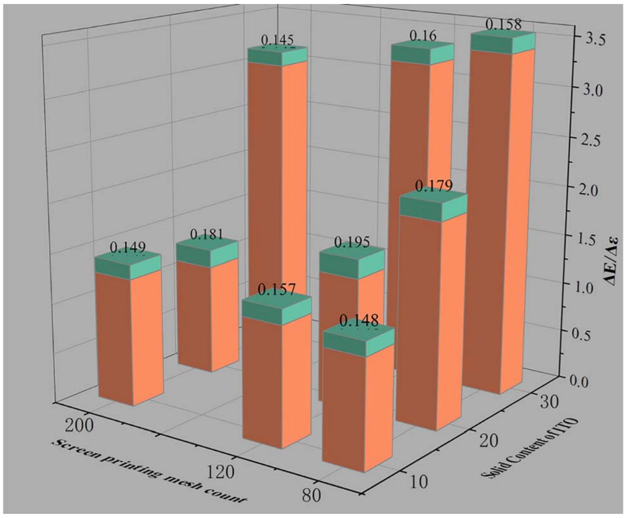

Fig. 6 Color difference and emissivity of ITO screen printing ink.

ITO screen printing ink was prepared in accordance with the method presented in Section 2.2. Its chromatic value and reflectivity at 8–14 μm are listed in Table 1.

The above calculation results show that ITO and ITO film have low emissivities within the wavelength range of 8–14 μm.[30,31] The data in Table 1 show that the emissivity of the prepared ITO ink is not excessively low likely due to the following two aspects: first, the ink is compatible with optical properties. The emissivity of the paint for optical camouflage is high, and adding ITO can reduce system emissivity. Meanwhile, obtaining the emissivity of ITO itself is difficult. Second, the physical and mechanical properties of the connection material should receive attention, and realizing complete infrared transparency is impossible. This study focuses on how ITO affects the optical camouflage performance of optical paints and reduction in infrared emissivity. The color differences between the ITO ink and medium green as well as the emissivity difference at 8–14 μm were calculated in accordance with the data in Table 1 and plotted in Fig. 6. After ITO ink was printed onto the surface of high-strength polyester fabric through 80-, 120-, and 200-mesh screen printing plates, the color difference with medium green is controlled within 3, and the emissivity reduction exceeds 0.13. The emissivity of the original medium green ($L = 39.58$, $a = -6.37$, $b = 17.01$) has decreased by one level. To summarize, the prepared ITO ink can be used as an optically compatible infrared camouflage ink.

4. Conclusions

The geometric structure of In_2O_3 that contains 80 atoms is first optimized on the basis of first principle theory. For the optimized dominant crystal $In_{32-x}Sn_xO_{48}$, different amounts of Sn atoms ($x = 1, 2, 3$) are added to the defect-free crystal to simulate ITO with different doping ratios of Sn atoms (3.125%, 6.25%, and 9.375%). The energy band structures, optical properties, and infrared absorption spectra of the crystal when $x = 0, 1, 2, 3$ are obtained. The results show that ITO retains its transparency in the waveband range of 303–1200 nm when $x = 3$ (Sn atom doping ratio of 9.375%). Moreover, it has strong absorptivity for the short waveband (wavelength < 303 nm) or ultraviolet band. It has high reflectivity for the long waveband (wavelength > 1200 nm) or infrared waveband. In accordance with calculation results, ITO with a Sn doping ratio of 9.375% is selected to prepare ink. ITO nanodispersion liquid (9.375%) is mixed with medium green optical camouflage coating to prepare ITO silkscreen printing ink for fabrics through modification. Later, the ink layer is prepared by coating the ITO ink onto the surface of high-strength polyester fabric through silkscreen printing. The experimental results show that the ink film can reduce the emissivity of the far infrared waveband at 8–14 μm by more than 0.13 without changing the optical properties of the medium green camouflage coating in the visible waveband.

On the basis of the fundamental material structure, this study interprets the camouflage mechanism of ITO in different wavebands through the calculation results of first principle theory from the perspective of quantum mechanics. Furthermore, the camouflage mechanism of ITO is verified by coating the prepared ink onto the surface of fabric. The results of this research can guide the applications of ITO in the field of camouflage. Future studies will explore how to further decrease the emissivity of ITO ink and develop other colors of ITO ink.

Author contributions

Conceptualization: Feifei Xiao and Weidong Xu. Data curation: Feifei Xiao, Bentian Hao, and Haibao Yu. Methodology: Feifei Xiao and Heng Liu. Resources: Heng Liu and Hao Li. Writing – original draft: Feifei Xiao; writing – review & editing: Feifei Xiao and Weidong Xu.

Conflicts of interest

The authors declare that they have no known competing financial interests or personal relationships that could have appeared to influence the work reported in this paper.

Acknowledgements

This research was funded by "Development and Engineering Application of Multispectral Compatible Camouflage Materials" (grant number 62122062205).

References

1 L. Wang, Y. Yang, X. Tang, *et al.*, Combined multi-band infrared camouflage and thermal management *via* a simple multilayer structure design, *Opt. Lett.*, 2021, **46**(20), 5224–5227.

2 H. Zhu, Q. Li, C. Tao, *et al.*, Multispectral camouflage for infrared, visible, lasers and microwave with radiative cooling, *Nat. Commun.*, 2021, **12**(1), 1805.

3 G. Liang, Y. Xiao, J. Zhang, *et al.*, Optimizing the emissivity regulation performance of a multilayer adaptive infrared

camouflage structure based on transport ability control of an ionic liquid, *Appl. Surf. Sci.*, 2023, **614**, 156145.

4 G. C. Ispas, V. Raditoiu, A. Raditoiu, *et al.*, Colored coating materials with spectrally selective reflectance for woodland camouflage textile fabrics, *Proceedings*, 2019, **29**(1), 61.

5 J. Yu and Z. Y. Hu, Study on Tent Cloth Materials for Desert Type Camouflage, *Adv. Mater. Res.*, 2012, **590**, 134–137.

6 F. Bollino and M. Catauro, Sol-Gel Technology to Prepare Advanced Coatings, *Photoenergy and Thin Film Materials*, 2019, pp. 321–378.

7 M. Wegener, D. Eckert and A. Roosen, Manufacture of sub-μm thin, particulate-based ITO layers by roller coating, *J. Eur. Ceram. Soc.*, 2015, **35**(8), 2321–2332.

8 Z. Chen, X. Qin, T. Zhou, *et al.*, Ethanolamine-assisted synthesis of size-controlled indium tin oxide nanoinks for low temperature solution deposited transparent conductive films, *J. Mater. Chem. C*, 2015, **3**(43), 11464–11470.

9 T. ChonanH. KunoFine particles of antimony tin oxide for sunscreen, dispersion thereof for sunscreen material formation, sunscreen material and transparent base material for sunscreen*AU Pat.*, 2003246172A, 2004.

10 J. Xu, J. B. Liu, B. X. Liu, *et al.*, Design of n-type transparent conducting oxides: the case of transition metal doping in In_2O_3, *Adv. Electron. Mater.*, 2018, **4**(3), 1700553.

11 C. Freysoldt, B. Grabowski, T. Hickel, *et al.*, First-principles calculations for point defects in solids, *Rev. Mod. Phys.*, 2014, **86**(1), 253.

12 S. J. Clark, M. D. Segall, C. J. Pickard, *et al.*, First principles methods using CASTEP, *Z. Kristallogr. - Cryst. Mater.*, 2005, **220**(5–6), 567–570.

13 P. Wisesa, K. A. McGill and T. Mueller, Efficient generation of generalized Monkhorst-Pack grids through the use of informatics, *Phys. Rev. B*, 2016, **93**(15), 155109.

14 R. Kingsbury, A. S. Gupta, C. J. Bartel, *et al.*, Performance comparison of r2SCAN and SCAN metaGGA density functionals for solid materials *via* an automated, high-throughput computational workflow, *Phys. Rev. Mater.*, 2022, **6**(1), 013801.

15 J. P. Perdew, J. A. Chevary, S. H. Vosko, *et al.*, Atoms, molecules, solids, and surfaces: applications of the generalized gradient approximation for exchange and correlation, *Phys. Rev. B: Condens. Matter Mater. Phys.*, 1992, **46**(11), 6671.

16 S. Grimme, J. Antony, S. Ehrlich, *et al.*, A consistent and accurate *ab initio* parametrization of density functional dispersion correction (DFT-D) for the 94 elements H-Pu, *J. Chem. Phys.*, 2010, **132**(15), 154104.

17 D. R. Hamann, M. Schlüter and C. Chiang, Norm-conserving pseudopotentials, *Phys. Rev. Lett.*, 1979, **43**(20), 1494.

18 R. R. Pela, M. Marques and L. K. Teles, Comparing LDA-1/2, HSE03, HSE06 and G0W0 approaches for band gap calculations of alloys, *J. Phys.: Condens. Matter*, 2015, **27**(50), 505502.

19 H. J. Monkhorst and J. D. Pack, Special points for Brillouin-zone integrations, *Phys. Rev. B: Solid State*, 1976, **13**(12), 5188.

20 I. Hamberg and C. G. Granqvist, Evaporated Sn-doped In_2O_3 films: basic optical properties and applications to energy-efficient windows, *J. Appl. Phys.*, 1986, **60**(11), R123–R160.

21 A. I. Cocemasov, V. I. Brinzari and D. L. Nika, Energetic, structural and electronic features of Sn-, Ga-, O-based defect complexes in cubic In_2O_3, *J. Phys.: Condens. Matter*, 2020, **32**(22), 225703.

22 G. B. González, *et al.*, Neutron diffraction study on the defect structure of indium-tin-oxide, *J. Appl. Phys.*, 2001, **89**(5), 2550–2555.

23 N. Nadaud, N. Lequeux, M. Nanot, *et al.*, Structural studies of tin-doped indium oxide (ITO) and $In_4Sn_3O_{12}$, *J. Solid State Chem.*, 1998, **135**(1), 140–148.

24 N. Balasubramanian and A. Subrahmanyam, Electrical and optical properties of reactively evaporated indium tin oxide (ITO) films-dependence on substrate temperature and tin concentration, *J. Phys. D: Appl. Phys.*, 1989, **22**(1), 206.

25 A. Klein, C. Körber, A. Wachau, *et al.*, Transparent conducting oxides for photovoltaics: manipulation of Fermi level, work function and energy band alignment, *Materials*, 2010, **3**(11), 4892–4914.

26 A. Klein, C. Körber, A. Wachau, *et al.*, Transparent Conducting Oxides for Photovoltaics: Manipulation of Fermi Level, Work Function and Energy Band Alignment, *Materials*, 2010, **3**, 1–2.

27 F. C. Zhang, Z. Y. Zhang, W. H. Zhang, *et al.*, The first-principle calculation of electronic structure and optical properties of In_2O_3, *Acta Chim. Sin.*, 2008, **66**(16), 1863.

28 J. J. Greffet, P. Bouchon and G. Brucoli, *et al.*, Generalized Kirchhoff law, *arXiv*, 2016, preprint, arXiv:1601.00312, DOI: **10.48550/arXiv.1601.00312**.

29 W. S. Mokrzycki and M. Tatol, Colour difference ΔE-A survey, *Mach. Graph. Vis.*, 2011, **20**(4), 383–411.

30 S. C. Dixon, D. O. Scanlon, C. J. Carmalt, *et al.*, n-Type doped transparent conducting binary oxides: an overview, *J. Mater. Chem. C*, 2016, **4**(29), 6946–6961.

31 A. S. A. C. Diniz, The effects of various annealing regimes on the microstructure and physical properties of ITO (In_2O_3:Sn) thin films deposited by electron beam evaporation for solar energy applications, *Renewable Energy*, 2011, **36**(4), 1153–1165.